ENGINEERING

Wearable bioadhesive ultrasound shear wave elastography

Hsiao-Chuan Liu[1,2]*†, Yushun Zeng[3]†, Chen Gong[3]†, Xiaoyu Chen[2], Piotr Kijanka[4], Junhang Zhang[3], Yuri Genyk[5], Hisham Tchelepi[6], Chonghe Wang[2], Qifa Zhou[1,3]*, Xuanhe Zhao[2,7]*

Acute liver failure (ALF) is a critical medical condition defined as the rapid development of hepatic dysfunction. Conventional ultrasound elastography cannot continuously monitor liver stiffness over the course of rapidly changing diseases for early detection due to the requirement of a handheld probe. In this study, we introduce wearable bioadhesive ultrasound elastography (BAUS-E), which can generate acoustic radiation force impulse (ARFI) to induce shear waves for the continuous monitoring of modulus changes. BAUS-E contains 128 channels with a compact design with only 24 mm in the azimuth direction for comfortable wearability. We further used BAUS-E to continuously monitor the stiffness of in vivo rat livers with ALF induced by ᴅ-galactosamine over 48 hours, and the stiffness change was observed within the first 6 hours. BAUS-E holds promise for clinical applications, particularly in patients after organ transplantation or postoperative care in the intensive care unit (ICU).

INTRODUCTION

Fulminant hepatic failure, also known as acute liver failure (ALF), is defined as a severe liver injury resulting in the onset of hepatic encephalopathy within 8 weeks of the initial symptoms in patients without underlying liver disease (1). ALF has a high mortality rate of approximately 80% due to massive short-term cell death (2, 3). This condition can occur as a result of various etiologies such as viral hepatitis (hepatitis A and E and hepatitis B), neoplastic infiltration, heart failure, mycotoxicosis, drug toxicity (4, 5), or complications of liver transplantation (1, 6). The survival rate of patients with ALF after 1 month is merely 23% if appropriate procedures such as liver transplantation or intensive care medicine are not immediately taken (7, 8). Even after liver transplantation, postoperative complications may still lead to acute liver graft dysfunction (6, 9) and high premature mortality (10). Therefore, prompt prognostic evaluation plays an important role in performing timely intensive care treatment of ALF, allowing graft salvage, and managing postoperative complications in the intensive care unit (ICU) (3).

The gold standard for prognosis models of ALF is mainly based on the histological examination of liver tissue biopsies, laparoscopy for liver surface evaluation, and laboratory markers (11). However, these methods are time-consuming, exist a certain level of risks due to invasive procedures, and could be impractical for critically ill patients (12). Several studies have been reported that liver stiffness is a promising prognosis marker for early detection of ALF (4, 8, 12–15). Critically ill patients with ALF in the ICU have shown a substantial increased liver stiffness (Young's modulus of approximately 27 kPa) compared to healthy controls (Young's modulus of approximately 3.8 to 6 kPa) (4, 8, 15). Ultrasound shear wave elastography (SWE) is a fast and noninvasive technique used to evaluate the stiffness of internal organs (13–15). However, an intrinsic limitation of conventional ultrasound elastography is that it requires clinicians to handhold ultrasound probes on patients during examinations, making it unable to continuously monitor changes in liver stiffness over the course of rapidly changing diseases.

The concept of wearable ultrasound can be traced back as early as 2005 when a pair of ultrasound transducers was implanted into the fracture region of mature sheep to monitor and accelerate the healing process of fractured long bones (16). Over the past decade, with the rapid growth of soft materials, wearable ultrasound devices have been extensively developed for imaging internal organs and evaluating various physiological features in biomedical applications such as measuring central blood pressure (17), assessing deep-tissue hemodynamics (18), monitoring cardiac functions (19), and continuously imaging diverse organs (20). However, these methods are primarily focused on imaging structures of biological tissues, not available for elastography measurements (table S1).

A recent report introduced a wearable device based on a stretchable ultrasound probe for measuring muscle stiffness using a compression-based excitation method (21). However, this method has limitations when it comes to the continuous measurement of stiffness of internal organs such as liver (table S1). The compression-based approach requires an additional tool, such as a finger or an actuator, to induce mechanical excitation; it is impractical to repeatedly compress one location of the skin over the course of the diseases. Additionally, compressing the skin may be unable to mechanically excite internal organs such as the liver and thus unsuitable for measuring their moduli. Furthermore, mechanical compression can distort the acoustic beam and stretchable ultrasound probe, which dramatically compromises the performances of ultrasound elastography (table S1). To the best of our knowledge, there is no ultrasound elastography technology that can provide continuous measurements of internal organ stiffness over a few hours. Therefore, the development of a wearable ultrasound elastography technology that can continuously monitor the evolution of liver stiffness at the early stage of ALF is essential to the prognosis evaluation of ALF.

[1]Department of Ophthalmology, Keck School of Medicine, University of Southern California, Los Angeles, CA 90033, USA. [2]Department of Mechanical Engineering, Massachusetts Institute of Technology, Boston, MA 02139, USA. [3]Alfred E. Mann Department of Biomedical Engineering, University of Southern California, Los Angeles, CA 90089, USA. [4]Department of Robotics and Mechatronics, AGH University of Krakow, Krakow 30059, Poland. [5]Division of Hepatobiliary, Pancreatic and Abdominal Organ Transplant Surgery, Keck School of Medicine, University of Southern California, Los Angeles, CA 90033, USA. [6]Radiology, Keck School of Medicine, University of Southern California, Los Angeles, CA 90033, USA. [7]Department of Civil and Environmental Engineering, Massachusetts Institute of Technology, Boston, MA 02139, USA.
*Corresponding author. Email: hsiaochu@usc.edu (H.-C.L.); qifazhou@usc.edu (Q.Z.); zhaox@mit.edu (X.Z.)
†These authors contributed equally to this work.

In this study, we report the wearable bioadhesive ultrasound elastography (BAUS-E) capable of continuously measuring liver stiffness over a 48-hour period. This enables the evaluation of the rapid changes in liver stiffness associated with ALF for prognostic purposes. BAUS-E incorporates a thin transducer array with 128 channels and merely 24 mm in azimuth direction. The thin transducer array can generate acoustic radiation force impulse (ARFI) as an excitation source to produce shear waves for elastography measurements. The thin array is further adhered to the skin via a bioadhesive tough hydrogel couplant for continuous and wearable ultrasound elastography over 48 hours [20]. This bioadhesive hydrogel-elastomer hybrid couplant can maintain high water content (>90 wt %), high interfacial toughness (>500 J m^{-2}), and low acoustic attenuation (i.e., similar to commercial ultrasound gels) for continuous and wearable ultrasound elastography. The small aperture size of the BAUS-E device with the soft bioadhesive couplant provides a comfortable wearability. We systematically characterized the performances of BAUS-E by conducting transducer measurements, phantom studies, and numerical simulations. We further validated the performances of BAUS-E in comparison with a commercial ultrasound transducer. Additionally, we demonstrated that BAUS-E could continuously measure liver stiffness changes in rats with ALF induced by D-galactosamine (D-Gal) over 48 hours. We showed a significant correlation between the increase in liver stiffness measured by BAUS-E and ALF indicated by histopathological staining. BAUS-E could find extensive applications in clinics and ICU for noninvasive and continuous monitoring of the moduli of internal organs over the course of rapidly changing diseases for their early detection such as ALF.

RESULTS

Performance of wearable BAUS-E

The proposed BAUS-E not only features a smaller active area for the comfortable wearability but also exhibits the capability to produce sufficient energy for ARFI push, allowing it to generate shear waves (Fig. 1A) and provide the satisfied image quality for tracking particle displacements (Fig. 1B). For the comfortable wearability, the proposed BAUS-E can provide a field of view (FOV) of only 24 mm in the azimuth direction for wearing purposes with the same amount of 128 channels for both the commercial device (L7-4) and BAUS-E (Fig. 1C). This is due to the sophisticated fabrication technique with a 1λ pitch size. The bioadhesive couplant was placed on four locations, including the arm, neck, chest, and waist of 15 subjects for 48 hours for the wearing comfort test [20]. Most subjects reported no positive reactions (i.e., itchiness, irritation, dryness, or redness) at any location. Only one subject reported minor itchiness after 48 hours of continuous wearing. We further compared the wearing comfort of the bioadhesive couplant with six other couplants on the arms of the 15 subjects for 48 hours [20]. The commercial 3M VHB acrylic tape was used as a reference group. Feelings were then evaluated using the visual analog scale (VAS), ranging from 0 (most comfortable) to 10 (most uncomfortable). We reported that the BAUS couplant is the most comfortable, while the liquid and solid hydrogel couplants are the least comfortable. The details can be found in our previous research [20]. For sufficient energy for ARFI push, we have evaluated the particle displacement of the CIRS phantom generated by both the L7-4 commercial device (Fig. 2A) and BAUS-E (Fig. 2C) as the shear wave was traveling at 2 ms. The particle velocity induced by the commercial device shows 3.50 ± 0.67 mm/s and

3.02 ± 0.29 mm/s created by BAUS-E (velocity is the derivative of displacement with respect to time), which shows that BAUS-E can provide sufficient particle displacements to that created by the commercial device, demonstrating its ability to generate sufficient energy for shear wave propagation.

The physical BAUS-E was represented (Fig. 1C). BAUS-E was composed of an acoustic backing layer, a flexible printed circuit board (f-PCB), a 128-channel lead zirconate titanate (PZT) composite, a matching layer, and a bio-adhesive hydrogel layer (Fig. 1C and table S2). The electrode separation of each element was finely diced with the 20-μm diamond blade by a dicing saw to achieve 128 individual channels (Fig. 1D). The center frequency of BAUS-E was designed to be 7.5 MHz to strike a balance between the expected spatial resolution and the required energy for ARFI pushes. The 1 λ$_{water}$ pitch size (approximately 200 μm) and 20-μm kerf size were selected based on the optimized thickness-vibration mode theory, which provided the active area of BAUS-E to have approximately 4 mm in elevational direction and merely 24 mm in azimuth direction (Fig. 1C). This size provided a suitable size to achieve both a sufficient FOV for shear wave propagations and comfortable wearability.

To characterize the performance of the BAUS-E device, the pulse-echo response, peak-peak sensitivity, −6-dB fractional bandwidth, electrical impedance, lateral resolution, and axial resolution were measured. For the pulse-echo response, the 50th channel was randomly selected, and its center frequency was measured at 7.2 MHz (fig. S1A). Comparing with the PiezoCAD simulation result of the center frequency of 7.5 MHz, there is a good agreement between the measured and simulated center frequencies of BAUS-E (fig. S1B). The mean center frequency of BAUS-E across all 128 channels was determined to be 7.5 ± 0.26 MHz (fig. S1C). The electrical impedance and phase spectrum were also evaluated and compared with the simulation results. The impedance of the 50th channel was measured to be approximately 165 ohms (fig. S2A), which aligns well with the simulation result of 164 ohms (fig. S2B). The mean impedance of BAUS-E across all 128 channels was found to be 164.72 ± 2.76 ohms (fig. S2C), demonstrating close agreement with the simulation results.

To further assess the performance of BAUS-E, we evaluated the peak-peak sensitivity, −6-dB fractional bandwidth, lateral resolution, and axial resolution. The mean peak-peak sensitivity was determined to be −4.14 ± −2.36 dB for BAUS-E and −3.17 ± −1.51 dB for the commercial transducer (fig. S3A). The peak-peak sensitivity reflects the ability of an ultrasonic device to detect reflectors at a specific depth in a test material. A value closer to 0 dB indicates higher sensitivity of the ultrasonic device. Regarding the −6-dB fractional bandwidth, the mean fractional bandwidth was 37.44 ± 4.85% for BAUS-E and 44.34 ± 3.05% for the commercial transducer (fig. S3B). BAUS-E exhibited a comparable performance to the commercial transducer in terms of peak-peak sensitivity and −6-dB fractional bandwidth. For the resolution of BAUS-E in B-mode imaging (fig. S4A), the lateral resolution and the axial resolution (target at 13 mm), determined by the −6-dB full-width half-maximum (FWHM) beam profile, were approximately 0.13 mm (fig. S4B) and 0.36 mm (fig. S4C) using tungsten wire phantom, respectively. Theoretical calculations predicted lateral (Eq. 8) and axial resolutions of 0.14 and 0.39 mm, respectively, based on BAUS-E's center frequency of 7.5 MHz and aperture size of 24 mm. Our results demonstrate that the BAUS-E device exhibits performance close to the simulation results of the transducer design and is comparable to the commercial ultrasound transducer.
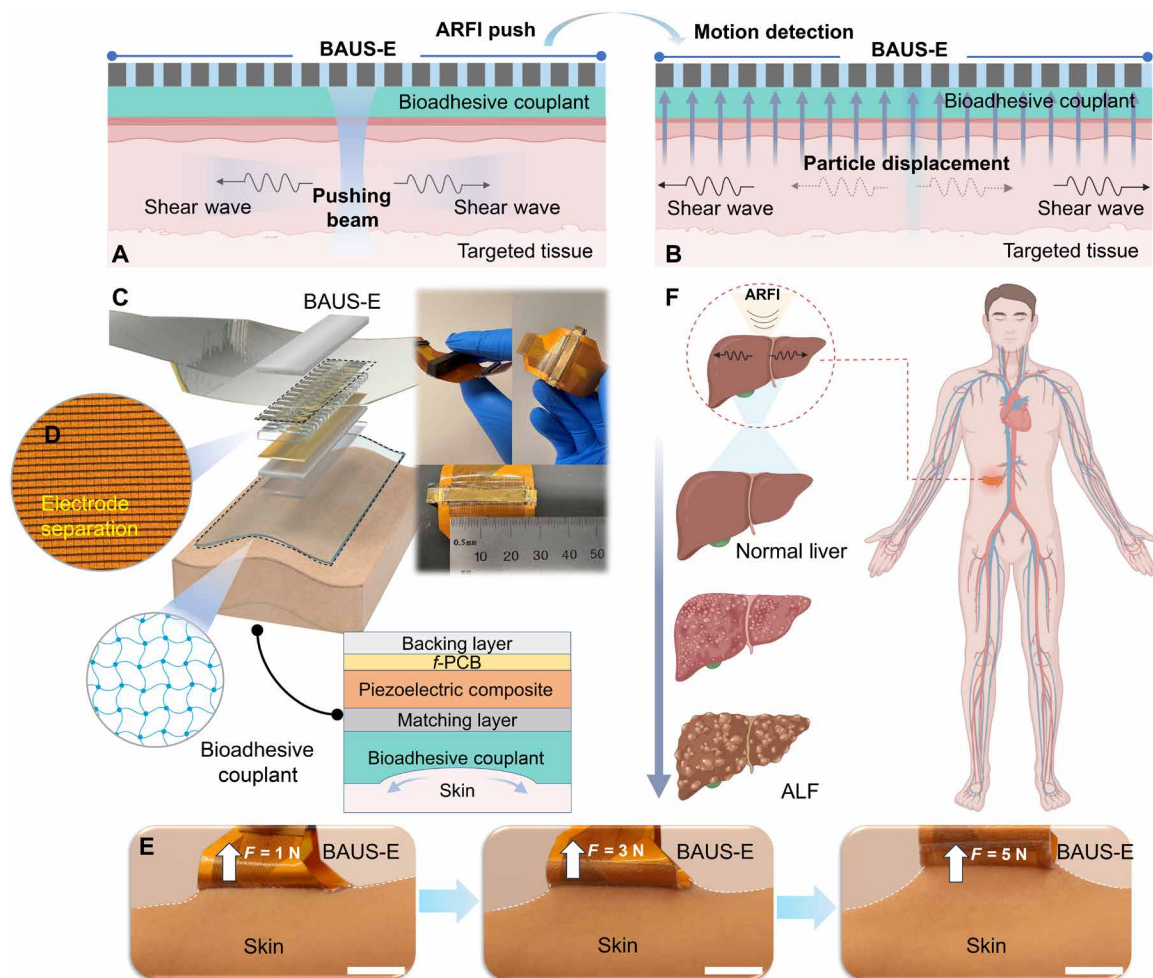
Fig. 1. Design and mechanism of wearable BAUS-E. (**A**) Schematic illustration of BAUS-E, showing its ability to provide an ARFI push to generate shear waves in biological tissues. (**B**) Schematic illustration of BAUS-E to demonstrate its capability to detect particle displacements induced by an ARFI push in biological tissues. (**C**) Schematic illustrations of the BAUS-E components, including the backing layer, flexible printed circuit board (*f*-PCB), piezoelectric composite, matching layer, and bioadhesive couplant. The bioadhesive couplant consists of a 95 wt % water-based tough hydrogel encapsulated by an elastomer membrane. A thin bioadhesive layer was further coated for maintaining a robust adhesion over 48 hours. (**D**) An electrode separation by a dicing saw was imaged using optical microscopy to show a 128-channel BAUS-E within only 24-mm aperture size. Scale bar, 10 mm. (**E**) The BAUS-E device adhered to the skin, demonstrating its ability to withstand a high pulling force from 1 to 5 N and maintain robust adhesion. Scale bar, 10 mm. (**F**) Schematic illustrations of BAUS-E used for elasticity measurements in acute liver failure (ALF) to monitor rapid changes in stiffness. Created using Biorender.com.

Systematic phantom evaluations of the elasticity and numerical simulations of BAUS-E

To evaluate the performance of BAUS-E in measuring mechanical properties using SWE, a systematic phantom study was conducted (Fig. 2). A commercial ultrasound phantom was used in this study to provide a ground truth value of shear wave velocity (C_g, group velocity), which was determined to be of 2.80 m/s provided by CIRS Inc. On the basis of Eq. 6, the Young's modulus was calculated as 23.52 kPa, assuming a density of 1000 kg/m^3 (provided by CIRS Inc.). This systematic experiment was divided into four different experimental conditions: SWE measured by the commercial ultrasound transducer with the conventional ultrasound coupling gel (control) (movie S1), SWE measured by the commercial ultrasound transducer interfaced with the bioadhesive couplant (movie S2), SWE measured by the wearable device with the conventional

ultrasound coupling gel (movie S3), and SWE measured by BAUS-E (move S4). To ensure consistency, the focus of the ARFI for both devices was placed at 10 mm below the phantom surface. The C_g measured by the commercial ultrasound transducer with the conventional ultrasound coupling gel and with bioadhesive couplant was 2.80 m/s (represented by the yellow dashed line, Fig. 2A) and 2.82 m/s (Fig. 2B), respectively. The C_g was 2.81 m/s (Fig. 2C) measured by the wearable ultrasound device with the ultrasound coupling gel and 2.78 m/s by BAUS-E (Fig. 2D). The mean C_g ($n = 10$) measured by the commercial transducer with the conventional ultrasound coupling gel, the commercial transducer with the bioadhesive couplant, the wearable device with the conventional ultrasound coupling gel, and BAUS-E was 2.81 ± 0.01 m/s (control), 2.82 ± 0.01 m/s, 2.79 ± 0.01 m/s, and 2.78 ± 0.04 m/s, respectively (Fig. 2M). On the basis of Eq. 6, the Young's modulus ranged between 23.18 kPa
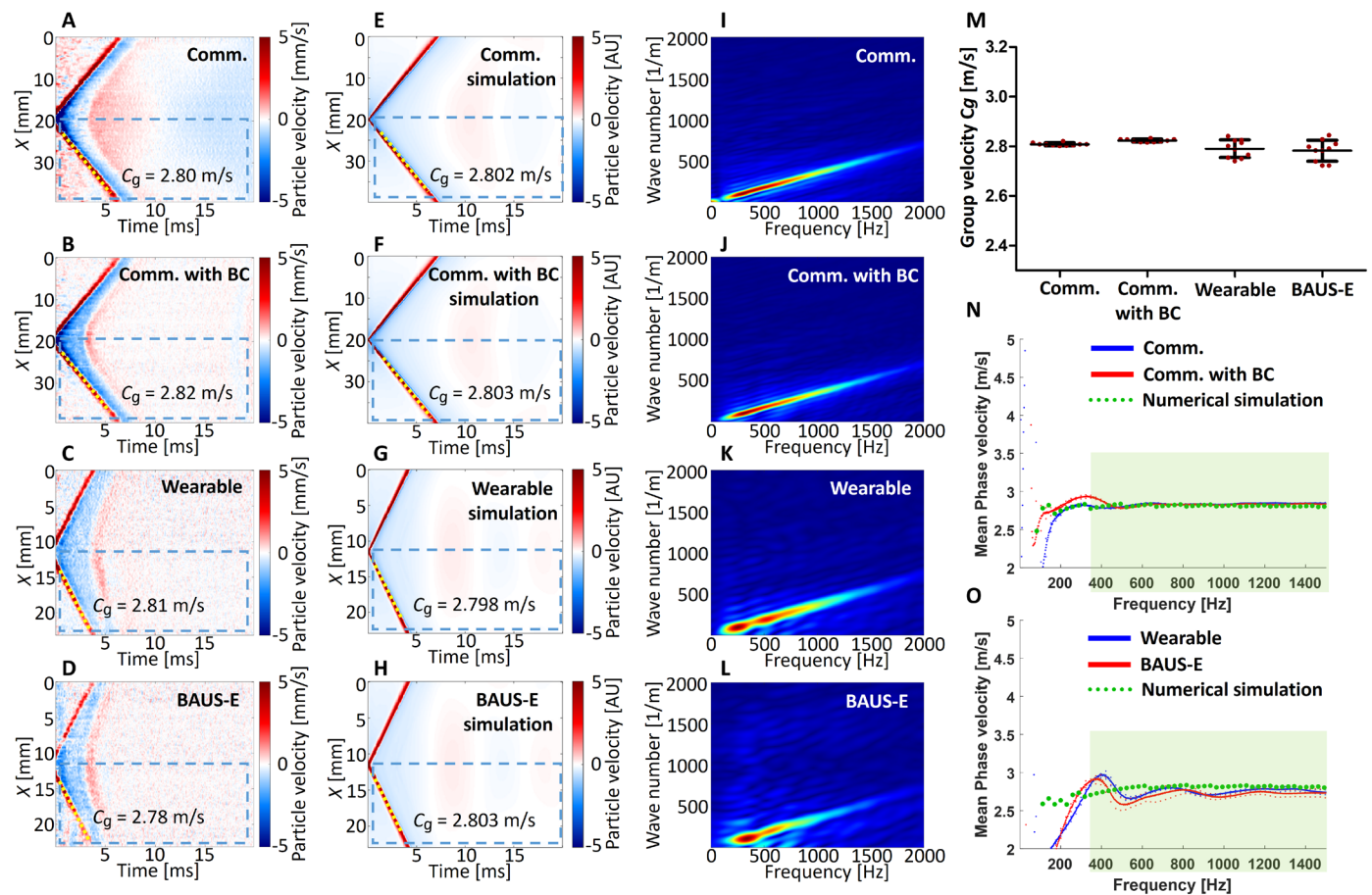
Fig. 2. Systematic phantom studies to evaluate the accuracy of shear waves. (**A** to **D**) Shear wave measurements in the time domain using different experimental conditions: (A) commercial ultrasound transducer coupled with clinical ultrasound gel, (B) commercial ultrasound transducer coupled with bioadhesive couplant, (C) proposed wearable device with clinical ultrasound gel, and (D) proposed wearable device with bioadhesive couplant, BAUS-E. (**E** to **H**) Numerical simulation results of shear waves corresponding to the four different experimental conditions, demonstrating good agreement with the experimental results. (**I** to **L**) 2D-FT analysis of the shear wave measurements for (A) to (D). (**M**) Mean shear wave velocities ($n = 10$) for the four different measurements presented with their SDs. (**N**) Dispersion curves for (A) and (B) in the frequency range of 400 to 1500 Hz compared with the numerical simulation results. (**O**) Dispersion curves for (C) and (D) in the frequency range of 400 to 1500 Hz compared with the numerical simulation results. Comm., commercial device; BC, bioadhesive couplant.

and 23.85 kPa, demonstrating good agreement with the ground truth value of 23.52 kPa. The systematic phantom experiments demonstrated that BAUS-E exhibited good performance for SWE. Furthermore, the phantom studies showed that the bioadhesive couplant did not interfere with the results of SWE due to its good acoustic impedance matching (*20*).

Numerical simulations were further used to validate the group velocity of shear waves in the four experimental cases as the secondary validation (fig. S5, A to D). The simulated ARFI focus was placed at a depth of 10 mm under the surface of the numerical phantom, mimicking the experimental setup. The ground truth value of the elastic property in the numerical phantom was set to 23.52 kPa, which matched the Young's modulus of the CIRS commercial phantom. The elastic property of bioadhesive couplant was set to 100 kPa based on our previous research (*20*). The simulated C_g was 2.802 m/s for the commercial ultrasound transducer with the conventional ultrasound coupling gel (control) (indicated by the yellow dashed line, Fig. 2E and fig. S5E) and 2.803 m/s for the transducer with the bioadhesive couplant (Fig. 2F and fig. S5F). The simulated C_g was

2.798 m/s measured by the wearable device with the ultrasound coupling gel (Fig. 2C and fig. S5G) and 2.803 m/s for BAUS-E (Fig. 2D and fig. S5H). According to Eq. 6, the Young's modulus ranged between 23.35 and 23.52 kPa, showing high consistency with the ground truth value of 23.52 kPa set in the numerical phantom. The results of the numerical simulations exhibited strong agreement with the experimental results across the four different experimental conditions for shear wave velocity measurements.

We further evaluated the dispersion curves of shear waves in the phantom study to analyze the frequency components of the measured shear waves in the time domain. The shear waves in the spatiotemporal map (indicated by the blue dashed rectangle, Fig. 2, A to H) were transformed into the frequency domain to calculate the *k*-space, which is a function of frequency (Hz) and wave number (1/m), allowing us to evaluate the shear wave velocity (C_p, phase velocity). The *k*-spaces from the experimental results (Fig. 2, I to L) and the numerical simulation results (fig. S5, I to L) were obtained using two-dimensional Fourier transform (2D-FT). On the basis of the *k*-space information, the mean wave dispersion curves were calculated for

the experimental and numerical simulation results (Fig. 2, N and O, and fig. S5, M to P). The mean C_p with the frequency range of 400 to 1500 Hz was determined to be 2.84 ± 0.01 m/s (corresponding to 24.19 kPa) (blue line, Fig. 2N) for the commercial ultrasound transducer with the conventional ultrasound coupling gel and 2.82 ± 0.01 m/s (corresponding to 23.85 kPa) (red line, Fig. 2N) for the transducer with the bioadhesive couplant. In the numerical simulation with the commercial ultrasound transducer, the mean C_p with the conventional ultrasound coupling gel was 2.81 ± 0.01 m/s (indicated by the green dot, Fig. 2N and fig. S5M), and with the bioadhesive couplant, it was 2.82 ± 0.01 m/s (corresponding to 23.68 kPa) (fig. S5N). On the other hand, for the wearable device with the conventional ultrasound coupling gel, the mean C_p was 2.76 ± 0.02 m/s (corresponding to 22.85 kPa) (blue line, Fig. 2O), and for BAUS-E, it was 2.74 ± 0.02 m/s (corresponding to 22.52 kPa) (red line, Fig. 2O). Comparing with the numerical simulations for the case with the wearable device, the mean C_p with the conventional ultrasound coupling gel was 2.80 ± 0.01 m/s (corresponding to 23.52 kPa) (green dot, Fig. 2O and fig. S5O) and 2.81 ± 0.01 m/s (corresponding to 23.68 kPa) for BAUS-E (fig. S5P). According to these three validation methods, BAUS-E demonstrated satisfactory performance in ARFI-based wearable ultrasound SWE.

Liver stiffness using BAUS-E reflects the severity of ALF in rats

The animal model with pharmacological induction of ALF using D-Gal was used. BAUS-E was used to continuously monitor the stiffness changes of rat livers with ALF over 48-hour period with measurements taken at 6-hour intervals (Fig. 3A). Thus, the liver stiffness changes in rats with ALF were measured at nine different time points. The experiments were repeated five times ($n = 5$), and each measurement at every time point consisted of three shear wave measurements, resulting in a total of 15 measurements at each time point. The C_g of rat livers at four different time points representing liver injuries (0, 12, 30, and 48 hours) and measured using BAUS-E were 1.23, 1.53, 1.80, and 2.42 m/s, respectively (Fig. 3B). The mean C_g of normal livers in rats (control) was 1.17 ± 0.08 m/s. At 6 hours after the injection of D-Gal, the mean C_g increased to 1.38 ± 0.05 m/s. Between the 12th and 30th hours, the mean C_g in rat livers with ALF gradually increased from 1.56 ± 0.05 m/s, 1.61 ± 0.07 m/s, 1.71 ± 0.09 m/s, to 1.82 ± 0.09 m/s, respectively. A significant increase in liver stiffness was observed between the 30th and 36th hours, with the mean C_g in rat livers with ALF increasing to 2.48 ± 0.12 m/s. After the 36th hour, the mean C_g reached a plateau around 2.5 m/s (Fig. 3C). There was a statistically significant difference in liver stiffness between normal livers and livers with ALF at each time point measurement ($P \leq 0.001$) (Fig. 3, C and D). The mean Young's modulus of normal livers in rats was 4.16 ± 0.55 kPa, which aligns well with the shear modulus measurements of 1.50 ± 0.10 kPa reported in well-established literature (22, 23). It is worth noting that the Young's modulus can generally be assumed as three times the shear modulus according to Eq. 5. The mean Young's modulus of livers after the injection of D-Gal gradually increased from 5.70 ± 0.44 kPa, 7.35 ± 0.48 kPa, 7.82 ± 0.74 kPa, 8.77 ± 0.92 kPa, to 10.00 ± 0.97 kPa in the SWE measurements between the 6th and 30th hours. The Young's modulus rapidly increased to 18.47 ± 1.88 kPa at the 36th hour, and liver stiffness remained stable until the 48th hour (18.08 ± 2.62 kPa at 42 hours and 18.17 ± 2.44 kPa at 48 hours) (Fig. 3D). These results demonstrated that using BAUS-E can effectively measure the liver

elasticity in rats with ALF as a valuable biomarker and can reflect the progression of ALF through rapid changes observed in continuous moduli measurements.

Histological stains reflect the tendency of the liver stiffness measured using BAUS-E

Three histological stains, hematoxylin and eosin (H&E) stain, Sirius red stain, and immunofluorescence (IF) stain, were conducted to examine the liver tissues in this study. The H&E stain revealed distinct levels of aggressiveness in ALF from 0 to 48 hours, highlighting morphological and structural changes (Fig. 4A). Compared to the control group, liver cell nuclei exhibited a degeneration trend with a radiation pattern after 12 hours of injection (indicated by black arrow, Fig. 4A). At the 30th hours, a noticeable fading in staining color with partial disappearance of liver cells was observed. By the 36th hour, several nuclei from the stained area along the appearance of cracks were observed (black arrow, Fig. 4A). At the 48th hour, nuclei within the stained region exhibited a nonuniform distribution, and boundaries of liver cells became blurred with extensive cracks. To quantify the aggressiveness of the liver in ALF, Sirius red and IF staining were performed to assess liver fibrosis. Sirius red staining, which binds to collagen fibers, is commonly used to detect and quantify collagen accumulation in liver tissues. Excessive collagen accumulation results in liver fibrosis, which impairs liver functionality. In the control group, a minor but evenly distributed presence of collagen fibers was observed around vascular walls (Fig. 4B). At the 12th hour after D-Gal injection, an increased distribution of collagen fibers around vascular walls was noticed. By the 36th hour, cracks accompanied by several collagen depositions were displayed (indicated by black arrow, Fig. 4B). At the 48th hour, the histological result exhibited numerous collagen fibers, indicating the progression of rat livers with ALF (indicated by black arrow, Fig. 4B). For IF staining, the level of α-smooth muscle actin (α-SMA) expression serves as a crucial indicator for quantitatively assessing the degree of liver fibrosis. In the control group, α-SMA expression was nearly undetectable (Fig. 4C). At the 12th hour, there were a few expressions of α-SMA observed around vascular walls (indicated by white arrow, Fig. 4C), followed by a substantial increase in expression at the 36th hour. Extensive distribution of liver fibrosis was exhibited at the 48th hour. The three histological examinations demonstrated high consistency, with large areas of cell necrosis, loss of hepatic structures, and perivascular inflammatory cell infiltration after D-Gal induction. The content of relative fibrosis (Fig. 4D) and relative collagen (Fig. 4F) from 0 to 48 hours was evaluated and showed a positive association with the level of progression of ALF. The regression analysis with Spearman correlation revealed that the Young's modulus of rat livers with stages of ALF measured using BAUS-E highly correlated with Sirius red staining results ($R = 0.94$, $P < 0.001$) (Fig. 4E) and α-SMA staining results ($R = 0.91$, $P < 0.001$) (Fig. 4G). These findings indicated that BAUS-E exhibited the reliable performance of the continuous SWE measurements and accurately reflected the changes in liver stiffness associated with ALF, which aligns with the histological results.

DISCUSSION

Previous studies have reported that liver stiffness, measured using conventional ultrasound SWE, is a reliable biomarker that significantly increases in critically ill patients with ALF compared to healthy controls (4, 13, 14, 24). Our continuous BAUS-E measurements
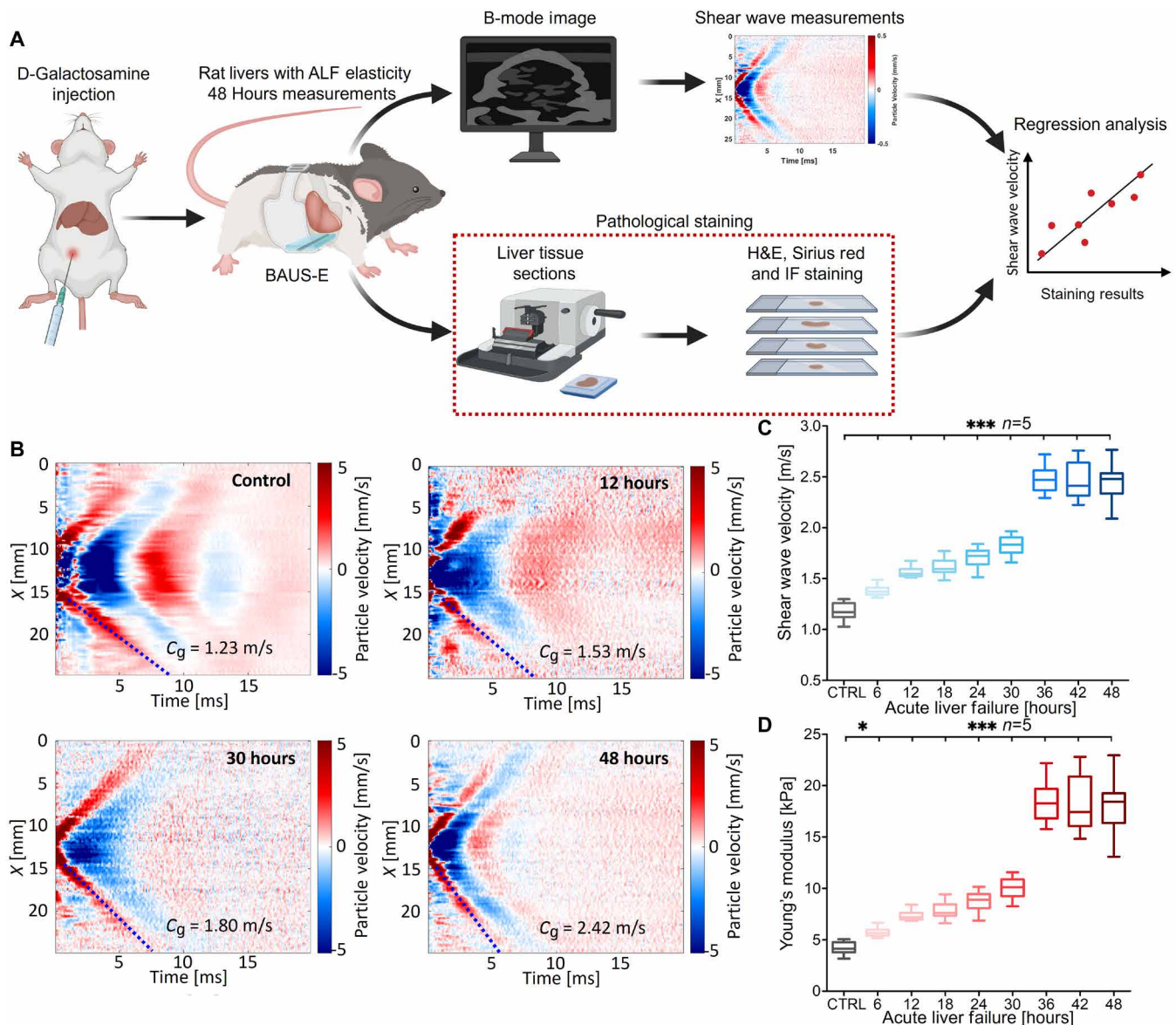
Fig. 3. Forty-eight–hour continuous monitoring of elasticity changes in rats with ALF using BAUS-E. (A) Schematic illustrations depicting the procedure for evaluating elasticity changes in rats with ALF. D-Gal was injected into nine rats via intraperitoneal injection to induce ALF. The elasticity of the rat liver was continuously monitored for 48 hours with 6-hour intervals using BAUS-E to obtain SWEs. At each 6-hour interval, one rat was randomly selected to sacrifice to obtain liver specimens for pathological staining, which corresponded to the timeline of the elasticity measurements. Regression analysis was performed to explore the relationship between pathological results and the shear modulus of rats with ALF. Created using Biorender.com. **(B)** Spatiotemporal maps illustrating shear wave velocities measured at 0, 12, 30, and 48 hours as examples. **(C)** Shear wave velocities were observed from 0 to 48 hours using BAUS-E. **(D)** Trend of Young's modulus changes in relation to the severity of rats with ALF over 48 hours. IF, immunofluorescence. $*P < 0.05$, $**P \leq 0.01$, and $***P \leq 0.001$.

exhibited a similar trend between the increase in liver stiffness and the progression of ALF after in vivo rat models received an intraperitoneal injection of D-Gal (Figs. 3D and 4). The increase in liver stiffness is closely correlated with hepatic fibrogenesis observed in H&E, Sirius red, and α-SMA staining (Fig. 4). We further observed significantly increased apoptosis and necrosis in the histological results associated with the progression of ALF (Fig. 4A), which is consistent with published literature (*21*). Existing prognostic models for ALF such as the model for end-stage liver disease (MELD) score have limitations in predicting outcomes in patients with ALF, mainly due

to high variation between laboratories and the challenge of standardization and replication worldwide (*12*). We demonstrated that the wearable BAUS-E can provide continuous measurements of live moduli over time and effectively differentiate stiffness changes in different stages of ALF progression compared to normal livers ($P < 0.001$) (Fig. 3, C and D). This has the potential for early prognosis prediction of ALF and could assist in evaluation of the graft condition after liver transplantation in ICU.

An interesting phenomenon was observed in the leap in stiffness between 30 and 36 hours (Fig. 3, C and D). A liver starts to lose its
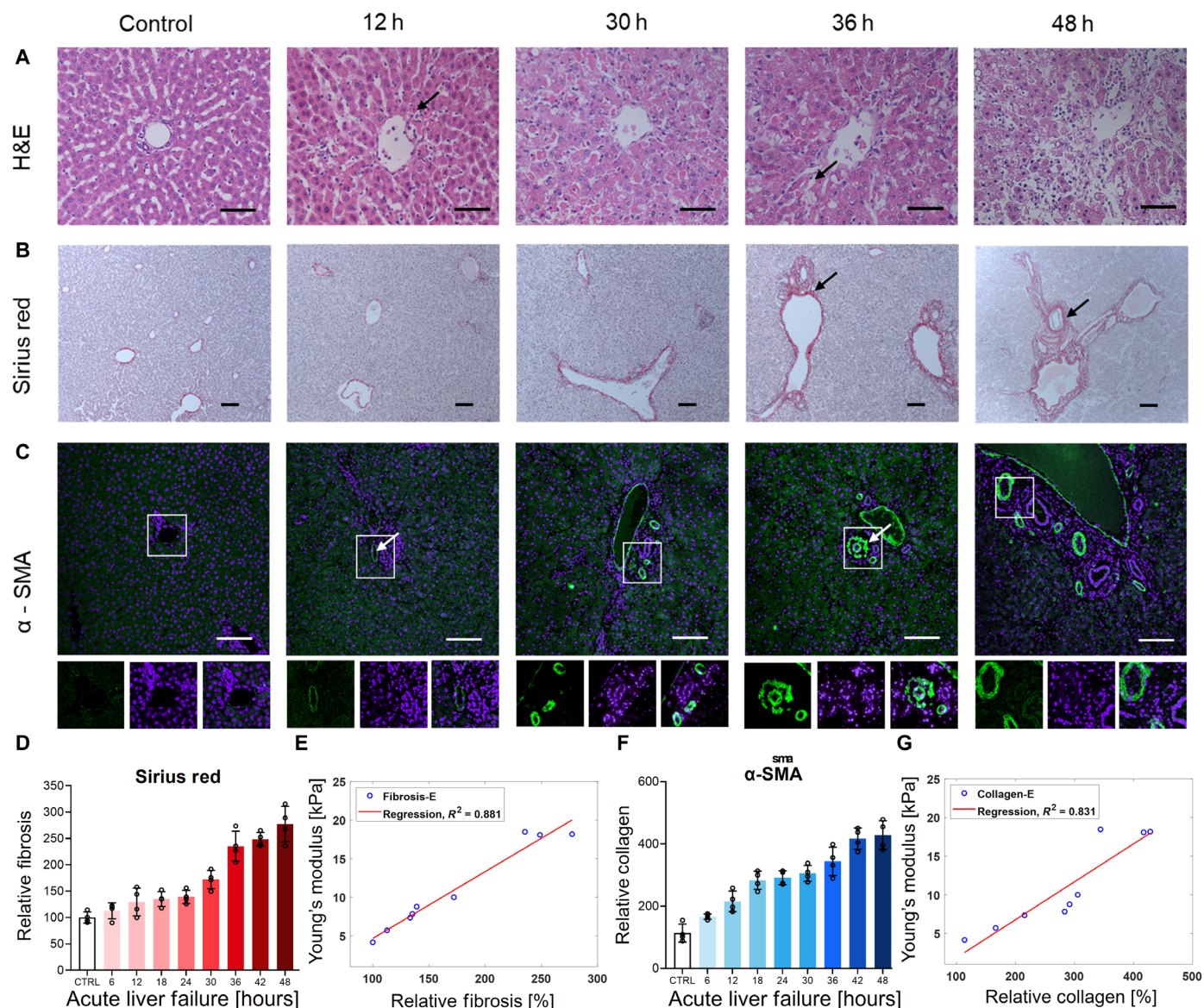
Fig. 4. Histological results of livers with ALF and regression analysis. (**A**) H&E staining, (**B**) Sirius red staining, and (**C**) α-SMA staining in rat liver tissues with fibrosis induced by D-Gal. (**D**) Quantification of hepatic fibrosis using Sirius red staining from 0 to 48 hours with 6-hour interval measurements. The control group was normalized to 100%. (**E**) Linear regression with Spearman analysis to evaluate the correlation between the Young's modulus measured using BAUS-E and the histological results using Sirius red staining, which was represented as the percentage of relative liver fibrogenesis at different time points (0 to 48 hours) with varying severity of ALF. (**F**) Quantification of liver fibrogenesis using α-SMA staining from 0 to 48 hours. (**G**) Linear regression analysis to evaluate the correlation between the Young's modulus measured using BAUS-E and the histological results of α-SMA staining. Scale bar, 100 μm.

function once a high dose of D-Gal is injected into a rat. The accumulated drug metabolizes into toxic substances in the body, leading to oxidative stress, inflammation, and apoptosis, thereby causing hepatocellular necrosis and ultimately liver damage (*25*). The metabolism of D-Gal in the liver depletes uridine triphosphate (UTP), uridine diphosphate (UDP), uridine monophosphate (UMP), and uridine sugar derivatives, leading to cellular energy depletion (*25*). Energy depletion results in cellular dysfunction, which causes cell damage and death. After post-injection of D-Gal, liver function–related indicators such as alanine aminotransferase (ALT) and aspartate aminotransferase (AST) begin to dynamically increase, blood

glucose starts to decrease, and coagulation function deteriorates. ALT and AST show a sudden increase within a certain time frame (e.g., 24 to 48 hours) (*26–29*). Furthermore, ALF is accompanied by a strong inflammatory response and progression to extrahepatic organ damage and dysfunction (*30, 31*). Several literatures report that levels of inflammatory cytokines and anti-inflammatory cytokines gradually increase from the beginning of the ALF, with significant growth observed between 48 and 72 hours (*27–29*), which indicates that the inflammatory response peaks in the later stages of liver cirrhosis, exacerbating tissue damage. Therefore, a leap in liver stiffness in ALF could be expected to occur, which may reflect such a rapid

change in real ALF patients. In this study, the histopathological changes between 30 and 36 hours could explain the leap in stiffness. A significant increase in liver fibrosis can be observed between 30 and 36 hours in Sirius red staining (Fig. 4B), and a complete collapse of the hepatic lobule structure was represented as the evidence of liver damage at 36 hours in H&E staining (Fig. 4A). However, predicting an exact moment of a leap could be challenging. Biomarkers with a sudden increase typically occur within a specific timeframe such as during the 24 to 48 hours (26–29), which indicates that it could happen at any time in the coming 1 to 2 days. However, using a slower increase in stiffness before a leap as an alert could serve as an early prognostic indicator before the situation worsens.

ARFI pushes that generate shear waves for SWE typically require longer pulse durations and higher pressures compared to conventional B-mode ultrasound imaging. Therefore, it is important to consider the biosafety aspects of SWE (32). In general, the biosafety of SWE should meet the same criteria as conventional B-mode ultrasound imaging. However, the biosafety of SWE is closely related to parameters such as the push peak voltage, push duration, and f-number ($f\#$) used during experiments. According to the regulations set by American Institute of Ultrasound in Medicine (AIUM) 1998 (33) and US Food and Drug Administration (FDA) (34), two parameters, mechanical index (MI) and $I_{SPTA,0.3}$, were considered for evaluating the biological effects of SWE using BAUS-E. In this study, we selected a push peak voltage of ±30 V, a push duration of 250 μs, and an $f\#$ of 1.5 for hydrophone measurements of BAUS-E to verify its acoustic safety. These parameters are consistent with those used in the animal studies. Hydrophone measurements revealed that the MI value of BAUS-E at the focal point of the ARFI push was 1.47 (fig. S6A) and $I_{SPTA,0.3}$ was 440.86 mW/cm^2 (fig. S6B), both of which were below the safety thresholds of 1.9 for MI and 720 mW/cm^2 for $I_{SPTA,0.3}$ specified by regulations. It should be noticed that the MI and $I_{SPTA,0.3}$ values may change if deeper regions of biological tissues are targeted for elasticity measurements using higher push peak voltages, longer push durations, or smaller $f\#$. This is a common consideration for commercial ultrasound machines as well (35).

The ARFI pushes in commercial ultrasound systems are typically performed at a distance of 4 to 4.5 cm from the linear array to achieve optimal liver stiffness measurements in clinical settings (36). However, for most wearable ultrasound devices, assessing the elastic properties of deep biological tissues remains challenging. This is because achieving a smaller $f\#$, which is necessary for a smaller aperture size to ensure comfortable wearability, can result in a weaker push force at deeper tissue regions (37). While mechanical compression-based methods have been reported to evaluate tissue stiffness up to 4 cm beneath the skin (21), larger loading forces may be required to avoid wave distortions when using stretchable ultrasound arrays (20). Consequently, assessing the elasticity of internal organs such as the liver could be difficult. Furthermore, mechanical compression methods often require additional excitation tools such as fingers or actuators, which makes continuous measurements challenging especially for the diseases that rapidly change (38). The proposed BAUS-E can provide the SWE for continuous monitoring of deep organ stiffness changes, which provides potential advantages over other methods.

We performed shear wave measurements at various depths using BAUS-E in the study (fig. S7). The phantom test involved ARFI pushes at depths of 20, 30, 40, and 50 mm beneath the surface of the phantom (fig. S7, A to D), and consistent results of C_g, approximately 2.8 m/s,

were obtained (fig. S7, I to L). In this study, the frequency range (7.5 MHz) of the proposed BAUS-E is designed for the small animal uses. Generally, the penetration depth of ultrasound can be approximately estimated as 200 to 300 wavelengths (39), corresponding to 40 to 60 mm. Despite having a smaller aperture size for comfortable wearability, BAUS-E demonstrated the capability to measure elasticity up to 50 mm (fig. S7L). BAUS-E would be sufficient for SWE evaluation in small animal research. On the other hand, for the potential ARFI energy deposition in deeper tissue (>6 cm) in translational applications for the clinical scenarios, the frequency of BAUS-E will need to decrease to approximately 2 to 5 MHz to make sure that the sufficient ARFI energy at the depth of 5 to 7 cm can be provided for translational applications such as for liver or kidney. A numerical simulation for BAUS-E with the center frequency of 3 MHz was provided to show that the 3-MHz BAUS-E can deal with the focus at 70 mm for the translational uses (fig. S8). This highlights the superior performance of BAUS-E to reach similar conditions as ARFI pushes performed in clinical settings, thus demonstrating its potential for translational applications (36).

In the phantom studies, we specifically selected a frequency range of 400 to 1500 Hz for evaluating the mean shear wave velocity and dispersion curve, excluding the low-frequency range from 0 to 400 Hz (Fig. 2, N and O). This selection was based on the consideration of the relationship between the shear wave wavelength and the aperture size of BAUS-E (40–42). The aperture size (FOV) of BAUS-E and the commercial device is approximately 24 and 40 mm, respectively. When the ARFI is placed in the middle of the device, the FOV is divided into two sections (fig. S9). Therefore, the useable FOV for the commercial device and BAUS-E was 20 and 12 mm, respectively. In the excitation region, no shear wave will be generated, and the shear wave velocity cannot be evaluated within this region (which could occupy a few millimeters in FOV), known as near-field effects (43). Consequently, the usable region for detecting shear wave propagation becomes even smaller—approximately 10 mm for BAUS-E and 18 mm for the commercial device. In shear wave evaluation, the wave should contain at least one complete cycle (one to two cycles would be better) to assure that the shear wave velocity can be correctly determined. Because the commercial CIRS phantom provides a homogeneous and elastic mechanical property, the shear wave phase velocity shows consistency at approximately 2.8 m/s throughout the frequency range. If we were to consider a frequency starting at 300 Hz, the shear wave wavelength would be approximately 9.3 mm, which is suitable for the commercial device due to its larger aperture size (40 mm) (Fig. 2, N and O). However, this wavelength would be very close to the usable region in BAUS-E (10 mm), potentially resulting in poor shear wave evaluation quality. To ensure accuracy, we considered the frequency starting at 400 Hz (wavelength of 7 mm) to ensure that the usable region of BAUS-E covers slightly more than one wavelength (Fig. 2O and fig. S9). For the commercial transducer, the dispersion curve in the low-frequency region (<400 Hz) was considered more reliable. To maintain consistency in the research, we kept the same frequency range for the dispersion curves measured using both BAUS-E and the commercial device when evaluating the mean phase velocity in the phantom study.

A higher variation from the measurement using BAUS-E was observed (Fig. 2O) compared to those using the commercial device. The reason for this higher variation is that the spatial distance covered by BAUS-E is smaller than that covered by the commercial

device. Specifically, for BAUS-E, only 10 mm of wave traveling data can be used to analyze the dispersion curve, compared with 18 mm for the commercial device (fig. S9). This difference in spatial coverage is the likely reason for the observed variations in the dispersion curve. An additional limitation in dispersion curve analysis is that frequencies lower than 400 Hz cannot be trusted due to the wavelength being larger than the usable FOV of BAUS-E.

The bioadhesive couplant can maintain low acoustic attenuation based on transmission tests. We tested the acoustic attenuation of bioadhesive couplant and compared with the commercially available gel adhesive pads. As shown in the experimental result (fig. S10), the attenuation coefficients of the BAUS-E couplant were measured to be from 0.038 to 0.124 dB/mm at frequencies from 1 to 10 MHz (black square). In comparison to the couplant without the elastomer layer, a similar attenuation coefficient from 0.037 to 0.121 dB/mm at frequencies from 1 to 10 MHz was evaluated (brown rhombus), showing that the couplant without the elastomer layer has almost the same acoustic attenuation as it does with the elastomer. Therefore, the reflection or absorption by the elastomer layer could be negligible. The tested result is reasonable to us because the thickness of the elastomer membrane is less than one-fourth of the ultrasound wavelength (approximately 40 μm only). We also compare the acoustic performance of the BAUS-E couplant with various commercially available products (fig. S11). The attenuation coefficients of the BAUS-E couplant (black square) demonstrate superior performance compared to the commercially available ultrasound couplants including Aquaflex couplant (gray triangle), Ecoflex Smooth-On silicone couplant (black rhombus), 3M VHB acrylic tape (red circle), and Olympus Aqualene (green pentagon) at frequencies from 1 to 10 MHz. BAUS-E exhibits the best performance with the lowest acoustic attenuation coefficient.

For the power assumption of the proposed BAUS-E device, the current BAUS-E device is driven by the Verasonics Vantage research ultrasound system; therefore, it would be difficult to exactly evaluate the power consumption of the BAUS-E device only because the Verasonics system almost dominates the total power consumption, which is 280 W (Verasonics Product Specification). However, a rough evaluation of the power consumption of BAUS-E could be evaluated. We assume that the phase of voltage and current [alternating current (AC)] is in phase ($\Delta\theta = 0°$), and the energy of the receiving cycle is far smaller than the ARFI push to be negligible. To consider an ARFI push voltage of ±30 V in this study, a push duration of 250 μs, and the measured impedance of 165 ohms (fig. S2B), the instantaneous power $p_i(t)$ can be presented as follows.

$$p_i(t) = v_{peak}\sin(wt) \times i_{peak}\sin(wt) \qquad (1)$$

where v_{peak} and i_{peak} are the peak value of the push voltage and current. According to the product-to-sum formulas, the instantaneous power $p_i(t)$ can be rewritten as:

$$p_i(t) = v_{rms}i_{rms} - v_{rms}i_{rms} \qquad (2)$$

where v_{rms} and i_{rms} are the root mean square of the voltage and current (which is defined as the peak value/$\sqrt{2}$), respectively; w is $2\pi f$; f is the center frequency of BAUS-E (7.5 MHz); and t is time. Because the push voltage of BAUS-E is AC, the power is considered as time dependent. However, the ARFI push duration is very short (only 250 μs); therefore, instantaneous power $p_i(t)$ can be approximately evaluated to be 2.3 W by substituting the parameters into Eq. 2.

In conclusion, we have presented the development of a wearable ultrasound device called BAUS-E, which can generate ARFI pushes to produce shear waves for continuous evaluation of the elastic modulus of organs and tissues. A limitation for the proposed device is that the current BAUS-E is connected to the Verasonics Vantage research ultrasound system. The I/Q data were transferred from Verasonics system to a personal computer, and MATLAB software was used for SWE processing. This is the first demonstration that a wearable ultrasound device can provide acoustic radiation force and SWE evaluation. In the near future, we plan to integrate the external power source and data processing into chips for portable style, creating an all-in-one BAUS-E for clinical use. BAUS-E holds great potential for expanding substantial applications of ultrasound wearable devices such as in patients undergoing organ transplantation in ICU, cancer research, and acute decompensated heart failure in clinical settings, in which the benefit of affixing an ultrasound device becomes especially evident.

MATERIALS AND METHODS
Fabrication of wearable BAUS-E
In the study, the development of the wearable ultrasound elastography device, BAUS-E, presented several design considerations to achieve optimal performance. To ensure good wearability, the device needed to have a small size. Additionally, it was essential to embed a sufficient number of channels for imaging, which in this case was 128 channels. Furthermore, the device needed to withstand high voltage driving to generate ARFI pushes, which posed a challenge during fabrication. To meet these requirements, a 7.5-MHz wearable BAUS-E device with a 128-element linear array was designed and fabricated. The 128 channels selected in this paper are based on the industrial standard of a linear array with a frequency range from 3 to 8 MHz. Most mainstream configurations for middle to high-level commercial medical ultrasound, such as GE and Philips, are equipped with 128 channels. For the core component of BAUS-E, a one- to three-composite PZT piezoelectric material with both-side electrodes (Blatek Industries Inc., Boalsburg, PA) was selected. The PZT material had a thickness of 140 μm, a pitch size of 200 μm, and a kerf size of 20 μm, which provide the aperture size of approximately 24 mm in azimuth dimension (table S2). These design specifications ensured that the width-to-thickness ratio was less than 0.7 (44), which is a crucial transducer design criterion. In the study, the width-to-thickness ratio was designed to be 0.57 (80 μm/140 μm). This ratio was chosen to generate a higher electromechanical coupling coefficient and enable pure thickness-mode resonance, resulting in better performance for ARFI-based elastography applications (44). A higher width-to-thickness ratio (>0.7) could induce different resonance vibration modes that interfere with the fundamental resonance mode, which could reduce the bandwidth and signal-to-noise ratio (SNR). Therefore, maintaining the appropriate width-to-thickness ratio was important for achieving optimal device performance.

The transducer performance of BAUS-E was simulated using a Krimboltz, Leedom, and Mattaei (KLM) equivalent circuit model in the PiezoCAD software (Sonic Concepts Inc., Bothell, USA) to explore the optimization of the electrical impedance, phase spectrum, and pulse-echo performance of BAUS-E before fabrication. On the basis of the simulation results, the two quarter-wavelength matching layers of BAUS-E were designed and added on the one side of the

PZT composite to compensate acoustic impedance mismatch between BAUS-E and biological tissues. For the designed array, a pitch size of 1 λ_{water} (approximately 200 μm in water) was chosen for the designed array to achieve higher imaging quality (*45–47*). The kerf size of the array element was set to 20 μm, and the composite kerf size was approximately 20 μm in this study based on the criterion $V_s/4f_c < 40$ μm (*48*), where V_s represents the shear velocity of the filled epoxy and f_c is the center frequency of the array. Therefore, the top electrode was scratch-diced along the kerf direction of the PZT composite to form a 128-channel electrode separation in the array.

The scratch-diced process was achieved by using a dicing saw (Tcar 864-1, Thermocarbon, Casselberry, FL). Afterward, the prepared composite component was bonded onto a customized *f*-PCB substrate. The alumina epoxy (Aluminum Oxide Powder, Buehler, IL, USA) was used to create a backing layer, which was adhered to the other side of the *f*-PCB to assemble a wearable ultrasound linear array. A bioadhesive hydrogel was then implanted on the surface of the wearable ultrasound linear array to form a wearable array patch, BAUS-E. To further evaluate BAUS-E, the electrical impedance and phase spectrum of each channel in BAUS-E were measured using an Impedance Analyzer (Agilent 4294A, Santa Clara, CA). The resonant frequency (f_r) and anti-resonant frequency (f_a) can be obtained to calculate the electromechanical coupling coefficient (k_t) using the following equation (*49*).

$$k_t = \sqrt{\frac{\pi}{2}\frac{f_r}{f_a}\tan\left[\frac{\pi}{2}\left(\frac{f_a - f_r}{f_a}\right)\right]} \qquad (3)$$

The pulse-echo performance, transducer sensitivity, and bandwidth at −6 dB of BAUS-E were tested using the Verasonics system (Vantage 256, Verasonics Inc., Kirkland, WA). By conducting these simulations and optimizing the transducer design parameters, the performance of BAUS-E could be tailored to meet the specific requirements of wearable ultrasound elastography.

SWE implementation

BAUS-E was compatible with the Verasonics system for implementing SWEs in phantom and animal studies. The Verasonics system was driven by MATLAB scripts (MATLAB R2022a release, MathWorks, Natick, MA, USA) that generated the necessary structures to achieve the desired action. In the phantom study, both BAUS-E and a commercial linear array (L7-4, Philips, MA) were used to scan a commercial ultrasound phantom (model 054GS, CIRS Inc., Norfolk, VA) for evaluating SWEs. The phantom provided a ground truth value of shear wave velocity as 2.8 m/s (Young's modulus $E = 24$ kPa provided by CIRS Inc.). The 32 elements in the middle of both transducers were used for the ARFI push, and all 128 elements were used for receiving particle displacements. The focal point of the ARFI for both devices was placed approximately 10 mm below the surface of the phantom, resulting in *f*# of approximately 1.5 for BAUS-E and 1.1 for the commercial array. In the phantom study using the commercial array, 1000 cycles of the ARFI push (push duration of 250 μs) were transmitted at 4.09 MHz, followed by plane wave compounding with three angles (−3°, 0°, +3°) performed immediately at 5 MHz for motion detection. To achieve a similar push duration in the phantom study using BAUS-E, an ARFI push with 1875 cycles (push duration of 250 μs) was used. The ARFI push was transmitted at 7.5 MHz, and the three angles of plane waves were immediately performed at the same frequency for motion detection.

In the animal studies, the focus of the ARFI push of BAUS-E was selected approximately 6 mm under the skin of the rats (near the middle of the liver). The ARFI push used the 20 elements in the middle of BAUS-E with a push duration of 250 μs. Subsequently, all 128 channels were activated for motion detection. The *f*# of BAUS-E in the animal study was approximately 1.5. In both the phantom and animal studies, the frame rate was set to 80 μs. Therefore, the effective frame rate after compounding was approximately 4.17 kHz (*50*).

For elasticity assessment, the in-phase/quadrature (I/Q) data were saved for offline analysis. The autocorrelation was used to calculate the particle velocity from the I/Q data, and the shear wave propagation was constructed via the spatiotemporal map (*51*). During the construction, a region of interest (ROI) was chosen from the axial displacement matrix. The ROI included the push row, five rows above the push, and the five rows below the push to average along the depth dimension over 0.5 mm. The maximum values of particle velocity at each time point were determined, and the shear wave group velocity C_g was obtained using a linear regression curve fitting method (*52*). To estimate the elastic properties of a biological tissue, simplifications of homogeneous, incompressible, and isotropic properties are commonly assumed, although a real biological tissue represents a complex heterogeneous, anisotropic, and nonlinear behavior. Therefore, the elasticity of the biological tissue can be treated as uniform distribution, and the tissue material response can be considered as non-orientation dependent (*38, 42*). Under these assumptions, C_g can be described as (*37, 53*).

$$C_g = \sqrt{\frac{G}{\rho}} \qquad (4)$$

where G is the shear modulus and ρ is the density of the medium, which was set as 1000 kg/m^3 in the study. Because of the assumption of incompressible and isotropic properties, the relationship between shear modulus and Young's modulus E can be expressed as

$$E = 3G \qquad (5)$$

Substituting Eq. 5 into Eq. 4, the relationship between C_g and E can be represented in the following way.

$$E = 3\rho c_g^2 \qquad (6)$$

To further validate how accuracy of measuring C_g using BAUS-E in the phantom studies, C_g was transformed from the time domain to the frequency domain using 2D-FT to calculate wave dispersions (*54*). 2D-FT was applied to the spatiotemporal map to obtain a frequency–wave number (*f-k*) domain distribution (*k*-space) of ultrasound shear waves. Shear wave phase velocity C_p was calculated by identifying the maximum peaks in the *k*-space using the equation $C_p = 2\pi f/k$, where f is the frequency and k is the wave number (*40–42*). A mean C_p over the frequencies from 400 to 1500 Hz on the dispersion curve was then computed. The aforementioned procedures were implemented using MATLAB R2022a software on a desktop computer with an Intel Core i7-7700 CPU at 3.60 GHz processor, 16 GB memory, and a 64-bit Windows 10 operating system.

Numerical simulations

To validate the proposed BAUS-E technique, numerical simulations were conducted using a staggered grid finite difference (SGFD) method. The SGFD scheme was implemented and used to generate particle velocity shear wave motion data. The SGFD scheme used

the velocity-stress first-order hyperbolic system of equations. To minimize undesired reflections from model boundaries, a complex frequency–shifted perfectly matched layer based on recursive integration was implemented (55). The Field II software package was used to simulate the ARFI push beam (56). For the validation in the phantom studies, a two-dimensional model with the elastic material property of the numerical phantom was considered with 23 mm width × 4 mm thickness for BAUS-E and 40 mm width × 20 mm thickness for the L7-4 transducer. The elastic domains were uniformly sampled at a spatial resolution of 0.1 mm. The thickness of the bioadhesive couplant was set to 1.2 mm based on measurements. On the basis of experimental results obtained using BAUS-E, the C_g in the numerical phantom was set to 2.8 m/s. The Young's modulus E of the numerical phantom can be approximately evaluated by the formula $3\rho C_g^2$ (37, 53) and was set to 24 kPa as the same value in the CIRS phantom, where C_g is the shear wave velocity, and the density of the materials ρ was set to 1000 kg/m³ in the simulation. To consider the boundary condition with the bioadhesive couplant, E was set to 100 kPa (corresponding to an approximate C_g of 5.77 m/s) as reported in a previous article (20). The simulation time step was set to 0.03 μs to ensure the stability of the numerical model. The ARFI excitation with a pulse duration of 250 μs was applied in the axial direction for both the commercial ultrasound transducer and BAUS-E in the phantom study (fig. S5). The focus of the ARFI push was set at 10 mm below the surface of the numerical phantom. The simulations were performed using parallel computation technology with modern graphics processing units (GPUs) and compute unified device architecture (CUDA). The calculations were conducted in MATLAB R2022a release on a desktop computer equipped with an Intel Core i7-6700 CPU at 3.40 GHz processor, 48 GB memory, and 64-bit Windows 10 Pro operating system, along with an NVIDIA GeForce RTX 2080 Ti graphics card. The computation time for the numerical simulations was approximately 25 min.

Fabrication of polyacrylamide hydrogel-elastomer hybrid bioadhesive couplant

The BAUS-E couplant contains a soft and tough hydrogel encapsulated by a bioadhesive elastomer membrane to form a hydrogel-elastomer hybrid. The polyacrylamide (PAAm)-chitosan tough hydrogel was synthesized by ultraviolet photo-polymerization of 3% (w/w) high–molecular weight chitosan, 12% (w/w) acrylamide, 0.1% (w/w) N,N'-methylenebisacrylamide, and 0.2% (w/w) α-ketoglutaric acid in a 1% (v/v) acetic acid solution. The obtained tough hydrogels were immersed in 1 M $CaCl_2$ solution for 24 hours to reach an equilibrium state. The bioadhesive membrane was designed as a sandwich structure with two layers of bioadhesive polyurethane and one layer of hydrophobic polyurethane. The bioadhesive polyurethane was synthesized by grafting polyacrylic acid chains and polyethylhexyl acrylate chains onto hydrophilic polyurethane. We used 30% (w/w) acrylic acid and 5% (w/w) 2-ethylhexyl acrylate to modify the hydrophilic polyurethanes. After the reaction, the mixture solution was dialyzed [cutoff M_n (number-average molecular weight) 3000 Da] against ethanol for 3 days and against water for three more days to obtain the bioadhesive polyurethane. A thin layer of bioadhesive polyurethane with 5% (w/w) 1-ethyl-3-(3-dimethylaminopropyl) carbodiimide (EDC) and 5% (w/w) N-hydroxysuccinimide (NHS) was spin-coated at 1500 rpm on a clean glass, and then hydrophobic polyurethane was spin-coated at 1500 rpm on the bioadhesive

polyurethane. Before the hydrophobic polyurethane layer was fully dried, another thin layer of bioadhesive polyurethane with 5% (w/w) EDC and 3% (w/w) NHS was spin-coated at 1500 rpm on the hydrophobic polyurethane layer. The film was then placed in airflow for 4 hours for drying to obtain the bioadhesive membrane. To fabricate the hydrogel-elastomer hybrid bioadhesive couplant, the hydrogel was tailored into the desired shape and size, and the adhesive membrane was adhered onto the hydrogel with a gentle press to avoid any bubbles. The BAUS-E transducer was firmly adhered to the couplant using a layer of 50% (w/w) hydrophilic polyurethanes in a 70% (v/v) ethanol and 30% (v/v) water solution. The fabrication of the bioadhesive hydrogel-elastomer hybrid couplant for BAUS-E followed the same procedure as the BAUS couplant, and the details can be found in (20).

Pulse-echo, bandwidth, impedance, and sensitivity measurements

The quartz material was used as a target to generate a complete reflection of the acoustic beams emitted by BAUS-E for the pulse-echo test. A 1D-FT was performed on the echo signal to calculate the frequency components presented in the spectrum. This evaluation enabled the determination of the center frequency as well as the higher-frequency f_H and low-frequency f_L at −6 dB. On the basis of the spectrum obtained, the fractional bandwidth FB was calculated using the following formula:

$$FB = 2\frac{f_H - f_L}{f_H + f_L} \quad (7)$$

Furthermore, the impedance of BAUS-E was measured using an impedance analyzer (Agilent 4294A, Santa Clara, CA, USA). The sensitivity refers to the ability of an ultrasonic system to detect reflectors at a given depth in a test material. A more sensitive transducer system is characterized by a stronger received signal from these reflectors. The sensitivity of BAUS-E was calculated using the equation $20\log V − \max(20\log V)$, where V represents the intensity of the echo signals.

Lateral and axial resolution measurement

To evaluate the lateral resolution and axial resolution of BAUS-E, a tungsten wire phantom with a diameter of 25 μm (purity 99.95%, California Fine Wire Co., Grover Beach, CA) was used. The theoretical calculation suggests that the best axial resolution is approximately two periods of a short pulse or the reciprocal of the center frequency, which can be approximated as two wavelengths (2λ). The lateral resolution can be described by the following formula (57):

$$\text{lateral resolution} = \frac{4\lambda d}{\pi a} \approx 1.2\lambda f\# \quad (8)$$

where d represents the focal length and a corresponds to the aperture size, which was 24 mm in this study.

Hydrophone measurement for acoustic energy verification

For the acoustic energy verification, hydrophone measurements were conducted to evaluate the acoustic energy safety. BAUS-E was mounted on a five-axis motorized stage and driven by the Verasonics system. The center frequency of 7.5 MHz with a burst cycle of 50 was used in the hydrophone measurement. The 20 elements in the middle of the device were selected for the ARFI push, and the focus was positioned at 6 mm under the surface of BAUS-E, which are the

same parameters in the animal studies. A hydrophone (HGL-0085, ONDA Inc., Sunnyvale, CA, USA) connected to a pre-amplifier (AH-2010-DCBNS, ONDA Inc., Sunnyvale, CA, USA) was used to measure the acoustic pressure generated by BAUS-E. BAUS-E was submerged inside a water tank filled with degassed water, and the hydrophone tip was suspended 6 mm below the surface of BAUS-E to measure the acoustic pressure from the ultrasonic transmitter. Two safety parameters were obtained to evaluate the biological effects of SWE including the spatial peak time-average intensity ($I_{SPTA,0.3}$) and MI. MI can be calculated using the formula:

$$\text{MI} = \frac{p_{r,0.3}}{\sqrt{f_0}} \qquad (9)$$

where $p_{r,0.3}$ is the peak rarefactional pressure at a rate of 0.3 dB cm^{-1} MHz^{-1} in MPa, as defined by AIUM 1998 guidelines (33), and f_0 represents the ultrasound center frequency in MHz. MI has been set the limit at 1.90 by US FDA (34). The equation for $I_{SPTA,0.3}$ in given by (34)

$$I_{SPTA,0.3} = (PII_{0.3} / PD_H) \cdot PD \cdot PRF \qquad (10)$$

Here, $PII_{0.3}/PD_H$ is defined as the spatial-peak pulse average intensity $I_{SPTA,0.3}$, PD_H is the pulse duration used for the hydrophone measurements, PD is the pulse duration used in the actual experiments, and PRF is the pulse repetition frequency. In this study, PD_H was 6.66 μs (50 cycles), PD was 250 μs (1875 cycles), and PRF was set to 1.11 mHz (corresponding to an ARFI push every 15 min for 1-hour continuous measurements). The parameter of $PII_{0.3}$ represents the pulse intensity integral defined by Eq. 11 (33)

$$PII_{0.3} = \frac{1}{10^4 \rho v} \int_{t_1}^{t_2} p_{0.3}^2(t) dt \qquad (11)$$

where ρ is the density of water (1000 kg/m^3), v is the speed of sound in water (1480 m/s), $p_{0.3}(t)$ is the derated pressure, and the 10^4 factor is used to convert from W/m^2 to W/cm^2. According to US FDA regulations, the limitation for $I_{SPTA,0.3}$ should not exceed 720 mW/cm^2.

Animal preparations

All experimental procedures were conducted in accordance with the approved guidelines and approved by the Institutional Animal Care and Use Committee (IACUC) at the University of Southern California (USC) under protocol numbers 21084 and 21493. Two-month-old male Long-Evan (LE) rats weighing 300 g were used for the study. The rats were housed in a controlled environment with 12-hour light/dark cycle at temperatures of 22° to 25°C with free access to food and water. During the SWE measurements, the rats were anesthetized with sevoflurane (3 to 4%) inhalation administered through a nose cone (58). A total of 50 rats were randomly divided into five groups, with each group containing 10 rats. The experimental period for each group spanned 2 days (48 hours), with elastography measurements using BAUS-E conducted at 6-hour intervals. This resulted in eight time points for measurements: 6, 12, 18, 24, 30, 36, 42, and 48 hours after the injection of D-Gal. Before the D-Gal injection, a control dataset was obtained by measuring liver stiffness using BAUS-E (0 hour). Therefore, a total of nine time points were measured for each group. The experiments were repeated five times (five groups, $n = 5$). In each group, three SWE measurements were

performed at each time point, which results in a total of 15 shear wave measurements for each time point after all five groups had been completed. In each group, the injection of D-Gal was performed simultaneously in the 10 rats. One rat from each group was used to monitor liver stiffness changes over the 48-hour period, while the remaining rats were sacrificed at specific time points corresponding to the SWE measurements (ranging from 0 to 48 hours) to obtain liver specimens for staining.

Pharmacological models

Hepatotoxins have been extensively used in the development of animal models with ALF (59). D-Gal is commonly used as the pharmacological agent for inducing ALF in preclinical models. The literatures reported that rats are known to be sensitive to D-Gal for inducing hepatic failure (59, 60). Therefore, rats were considered as the animal model to develop ALF in this study. Before injection, the D-Gal solution was sterilized using a 0.22-μm filter to prevent infections. After a 1-week acclimatization period, the rat liver injury model was induced by injecting D-Gal (G0500-5G, ≥99%, Sigma-Aldrich, St. Louis, MO) dissolved in saline. The dose used for the injection was 3 g/kg of body weight, which is known to render rats comatose within 36 to 48 hours due to ALF and leads to more than 90% mortality within 72 hours to mimic the symptoms of ALF (60).

Heart perfusion

For heart perfusion, rats were initially anesthetized with an intra-peritoneal injection of ketamine/xylazine at doses of 50 to 90 mg/kg and 5 to 10 mg/kg, respectively. The chest was opened to expose the heart, and a 1% solution of heparin sodium (0.2 ml) was injected into the left ventricle of the heart (61). A cannula was then inserted into the aorta via the left ventricle, and the right auricle was clipped after securing the cannula with a vascular clamp. The vasculature was first flushed rapidly with 150 ml of physiological saline solution, followed by perfusion fixation with 250 ml of 4% paraformaldehyde in 0.01 M phosphate-buffered saline (PBS) at a temperature of 4°C and pH 7.40. The entire process of the perfusion took approximately 40 min. During the perfusion process, the entry of paraformaldehyde into the rat's body may cause convulsions in the limbs and tail of the animal. The perfusion was considered complete when the liver turned pale. After perfusion, the liver was isolated and placed in a 4% paraformaldehyde fixative solution (PFS) for fixation and stored in a refrigerator at 4°C for subsequent histological analysis.

H&E staining

The liver specimens were embedded in paraffin, mounted on the microscope slides, and stained with H&E. The deparaffinization process was initiated by immersing the tissue sections in xylene for two cycles, with each cycle lasting 10 min. This was followed by two rounds of hydration using absolute alcohol, allowing 5 min for each round. The sections were then briefly immersed in 95% and 70% alcohol solutions for 1 min each, followed by rinsing in distilled water. Next, the sections were immersed in filtered Harris hematoxylin for 10 s. Afterward, the rack containing the sections was transferred to a beaker filled with tap water, and the tap water was exchanged until it became clear. The sections were then immersed in eosin stain for approximately 30 s. Repeatedly, the rack was transferred to a beaker with tap water, and the tap water was exchanged until it became clear. To dehydrate the sections, two cycles of

absolute alcohol immersion were performed, with each cycle lasting approximately 5 min. Following that, two cycles of xylene immersion, each lasting 5 min, were carried out to clear the sections. Last, the sections were mounted using a resin-based mounting medium.

Sirius red staining

The deparaffinization method was the same as that used for H&E staining. After that, Weigert's hematoxylin solution was applied to the sections and left for 10 min, followed by rinsing the slides under running tap water for an additional 10 min. The slides were then subjected to picro-Sirius red solution staining for 1 hour. After a quick rinse with distilled water, the sections were immersed in acetic acid solution for 1 min. The slides were vigorously shaken to remove most of the water. The dehydration method was the same as that used for H&E staining. Last, the sections were mounted using a resin-based mounting medium. All the necessary solutions were from the NovaUltra Sirius red stain kit (IW-3012, IHC-WORLD, USA).

IF staining of α-SMA

For immunostaining, all slides were deparaffinized, rehydrated, and antigen-retrieved using sodium citrate (pH 6.0). The sections were then incubated in blocking buffer consisting of 10% donkey serum and 0.2% Triton X-100 (Sigma-Aldrich, St. Louis, MO, USA) in PBS for 1 hour at room temperature. Subsequently, the slides were incubated with the primary antibody (Alpha SMA, Rabbit anti-Rat, 50-173-6008, Proteintech Group Inc., USA) at a dilution of 1:100 from Cell Signaling Technology (Danvers, MA) overnight at 4°C. After several washes with PBS, the slides were incubated with a fluorescent-labeled secondary antibody [Alexa Fluor 488 Goat anti-Rabbit IgG (H+L) Highly Cross-Adsorbed Secondary Antibody, PIA32731TR, Invitrogen, USA] for at least 1 hour at room temperature. Following staining, the slides were mounted with a fluorescent-enhanced mounting medium containing 4′,6-diamidino-2-phenylindole (DAPI) (Vector Laboratories, Burlingame, CA, USA). Images were captured using the Ultra viewer ERS dual-spinning disk confocal microscope (PerkinElmer, Waltham MA, USA) equipped with a C-Apochromat (Carl Zeiss, Thornwood, NY, USA) ×10 high dry lens, a C-Apochromat ×40 water immersion lens with a numerical aperture (NA) of 1.2, and an electron multiplier charge-coupled device cooled digital camera (Hamamatsu 12-bit camera, PerkinElmer, Waltham, MA, USA).

Statistical analysis

All results are reported as the mean ± SD using GraphPad Prism version 5 (GraphPad Software Inc., San Diego, USA). The D'Agostino and Pearson omnibus normality test and Shapiro-Wilk normality test were performed to access whether the data can be assumed to describe a normal distribution. Since the normality tests yielded a positive result in this study, we assumed that our data represented a normally distributed population. To compare multiple independent samples, we conducted a one-way analysis of variance (ANOVA) test with a significance threshold of $*P < 0.05$, $**P \leq 0.01$, and $***P \leq 0.001$ in the statistical analysis. Furthermore, Dunn's adjustment was implemented for adjusting the P values in more strict condition to account for multiple comparisons. To examine the correlation between Young's modulus of the liver in rats measured using BAUS-E and the histological results, the Spearman correlation test was used.

Supplementary Materials

This PDF file includes:
Figs. S1 to S11
Tables S1 and S2
Legends for movies S1 to S4
References

Other Supplementary Material for this manuscript includes the following:
Movies S1 to S4

REFERENCES AND NOTES

1. W. Bernal, J. Wendon, Acute liver failure. *N. Engl. J. Med.* **369**, 2525–2534 (2013).
2. H. H. Hussey, Fulminant hepatic failure. *JAMA* **226**, 1227 (1973).
3. M. Mendizabal, M. O. Silva, Liver transplantation in acute liver failure: A challenging scenario. *World J. Gastroenterol.* **22**, 1523–1531 (2016).
4. A. Dechene, J. P. Sowa, R. K. Gieseler, C. Jochum, L. P. Bechmann, A. El Fouly, M. Schlattjan, F. Saner, H. A. Baba, A. Paul, V. Dries, M. Odenthal, G. Gerken, S. L. Friedman, A. Canbay, Acute liver failure is associated with elevated liver stiffness and hepatic stellate cell activation. *Hepatology* **52**, 1008–1016 (2010).
5. N. Panchani, P. Schulz, J. Van Zyl, J. Felius, R. Baxter, E. T. Yoon, H. Baldawi, A. Bindra, S. K. Asrani, Liver stiffness and prediction of cardiac outcomes in patients with acute decompensated heart failure. *Clin. Transplant.* **36**, e14545 (2022).
6. A. H. M. Caiado, R. Blasbalg, A. S. Z. Marcelino, M. da Cunha Pinho, M. C. Chammas, C. da Costa Leite, G. G. Cerri, A. C. de Oliveira, T. Bacchella, M. C. C. Machado, Complications of liver transplantation: Multimodality imaging approach. *Radiographics* **27**, 1401–1417 (2007).
7. V. Arroyo, R. Moreau, P. S. Kamath, R. Jalan, P. Gines, F. Nevens, J. Fernandez, U. To, G. Garcia-Tsao, B. Schnabl, Acute-on-chronic liver failure in cirrhosis. *Nat. Rev. Dis. Primers.* **2**, 16041 (2016).
8. A. Gottlieb, A. Canbay, Liver stiffness and acute liver failure, in *Liver Elastography: Clinical Use and Interpretation*, S. Mueller, Ed. (Springer International Publishing, 2020), pp. 297–305.
9. E. V. Craig, M. T. Heller, Complications of liver transplant. *Radiology* **46**, 43–67 (2021).
10. R. Moreno, M. Berenguer, Post-liver transplantation medical complications. *Ann. Hepatol.* **5**, 77–85 (2006).
11. J. G. O'Grady, G. J. Alexander, K. M. Hayllar, R. Williams, Early indicators of prognosis in fulminant hepatic failure. *Gastroenterology* **97**, 439–445 (1989).
12. H. Kuroda, T. Abe, Y. Fujiwara, T. Nagasawa, Y. Suzuki, K. Kakisaka, Y. Takikawa, Contrast-enhanced ultrasonography-based hepatic perfusion for early prediction of prognosis in acute liver failure. *Hepatology* **73**, 2455–2467 (2021).
13. H. Kuroda, K. Kakisaka, T. Oikawa, M. Onodera, Y. Miyamoto, K. Sawara, R. Endo, K. Suzuki, Y. Takikawa, Liver stiffness measured by acoustic radiation force impulse elastography reflects the severity of liver damage and prognosis in patients with acute liver failure. *Hepatol. Res.* **45**, 571–577 (2015).
14. H. Kuroda, Y. Takikawa, M. Onodera, K. Kakisaka, Y. Yoshida, K. Kataoka, K. Sawara, Y. Miyamoto, K. Oikawa, R. Endo, K. Suzuki, Serial changes of liver stiffness measured by acoustic radiation force impulse imaging in acute liver failure: A case report. *J. Clin. Ultrasound* **40**, 99–104 (2012).
15. T. F. Karlas, C. Pfrepper, J. Rosendahl, C. Benckert, C. Wittekind, S. Jonas, J. Moessner, M. Troltzsch, H. L. Tillmann, T. Berg, V. Keim, J. Wiegand, Acoustic radiation force impulse (ARFI) elastography in acute liver failure: Necrosis mimics cirrhosis. *Z. Gastroenterol.* **49**, 443–448 (2011).
16. V. C. Protopappas, D. A. Baga, D. I. Fotiadis, A. C. Likas, A. A. Papachristos, K. N. Malizos, An ultrasound wearable system for the monitoring and acceleration of fracture healing in long bones. *IEEE Trans. Biomed. Eng.* **52**, 1597–1608 (2005).
17. C. Wang, X. Li, H. Hu, L. Zhang, Z. Huang, M. Lin, Z. Zhang, Z. Yin, B. Huang, H. Gong, S. Bhaskaran, Y. Gu, M. Makihata, Y. Guo, Y. Lei, Y. Chen, C. Wang, Y. Li, T. Zhang, Z. Chen, A. P. Pisano, L. Zhang, Q. Zhou, S. Xu, Monitoring of the central blood pressure waveform via a conformal ultrasonic device. *Nat. Biomed. Eng.* **2**, 687–695 (2018).
18. C. Wang, B. Qi, M. Lin, Z. Zhang, M. Makihata, B. Liu, S. Zhou, Y. H. Huang, H. Hu, Y. Gu, Y. Chen, Y. Lei, T. Lee, S. Chien, K. I. Jang, E. B. Kistler, S. Xu, Continuous monitoring of deep-tissue haemodynamics with stretchable ultrasonic phased arrays. *Nat. Biomed. Eng.* **5**, 749–758 (2021).
19. H. Hu, H. Huang, M. Li, X. Gao, L. Yin, R. Qi, R. S. Wu, X. Chen, Y. Ma, K. Shi, C. Li, T. M. Maus, B. Huang, C. Lu, M. Lin, S. Zhou, Z. Lou, Y. Gu, Y. Chen, Y. Lei, X. Wang, R. Wang, W. Yue, X. Yang, Y. Bian, J. Mu, G. Park, S. Xiang, S. Cai, P. W. Corey, J. Wang, S. Xu, A wearable cardiac ultrasound imager. *Nature* **613**, 667–675 (2023).
20. C. Wang, X. Chen, L. Wang, M. Makihata, H. C. Liu, T. Zhou, X. Zhao, Bioadhesive ultrasound for long-term continuous imaging of diverse organs. *Science* **377**, 517–523 (2022).

21. H. Hu, Y. Ma, X. Gao, D. Song, M. Li, H. Huang, X. Qian, R. Wu, K. Shi, H. Ding, M. Lin, X. Chen, W. Zhao, B. Qi, S. Zhou, R. Chen, Y. Gu, Y. Chen, Y. Lei, C. Wang, C. Wang, Y. Tong, H. Cui, A. Abdal, Y. Zhu, X. Tian, Z. Chen, C. Lu, X. Yang, J. Mu, Z. Lou, M. Eghtedari, Q. Zhou, A. Oberai, S. Xu, Stretchable ultrasonic arrays for the three-dimensional mapping of the modulus of deep *tissue*. *Biomed. Eng.* **7**, 1321–1334 (2023).

22. M. H. Wang, M. L. Palmeri, C. D. Guy, L. Yang, L. W. Hedlund, A. M. Diehl, K. R. Nightingale, In vivo quantification of liver stiffness in a rat model of hepatic fibrosis with acoustic radiation force. *Ultrasound Med. Biol.* **35**, 1709–1721 (2009).

23. G. Carbonell, J. D. Berna-Serna, L. Oltra, C. M. Martinez, N. Garcia-Carrillo, F. Guzman-Aroca, F. J. Salazar, J. Tudela, J. D. Berna-Mestre, Evaluation of rat liver with ARFI elastography: In vivo and ex vivo study. *PLOS ONE* **14**, e0217297 (2019).

24. A. Koch, A. Horn, H. Duckers, E. Yagmur, E. Sanson, J. Bruensing, L. Buendgens, S. Voigt, C. Trautwein, F. Tacke, Increased liver stiffness denotes hepatic dysfunction and mortality risk in critically ill non-cirrhotic patients at a medical ICU. *Crit. Care* **15**, R266 (2011).

25. S. Mehdi, F. U. Ahmad, A. H. Lodhi, U. Khurshid, A. A. Khalid, S. S. Sidiq, L. Hussain, M. S. Baig, Protective effects of p-CA against acute liver damage induced by LPS/D-GalN in Wistar albino rats. *Drug Des. Devel. Ther.* **16**, 3327–3342 (2022).

26. P. P. Cen, L. X. Fan, J. Wang, J. J. Chen, L. J. Li, Therapeutic potential of menstrual blood stem cells in treating acute liver failure. *World J. Gastroenterol.* **25**, 6190–6204 (2019).

27. L. Feng, Y. Wang, Y. Fu, A. Yimamu, Z. Guo, C. Zhou, S. Li, L. Zhang, J. Qin, S. Liu, X. Xu, Z. Jiang, S. Cai, J. Zhang, Y. Li, Q. Peng, X. Yi, G. He, T. Li, Y. Gao, A simple and efficient strategy for cell-based and cell-free-based therapies in acute liver failure: hUCMSCs bioartificial liver. *Bioeng. Transl. Med.* **8**, e10552 (2023).

28. W. J. Li, X. J. Zhu, T. J. Yuan, Z. Y. Wang, Z. Q. Bian, H. S. Jing, X. Shi, C. Y. Chen, G. B. Fu, W. J. Huang, Y. P. Shi, Q. Liu, M. Zeng, H. D. Zhang, H. P. Wu, W. F. Yu, B. Zhai, H. X. Yan, An extracorporeal bioartificial liver embedded with 3D-layered human liver progenitor-like cells relieves acute liver failure in pigs. *Sci. Transl. Med.* **12**, eaba5146 (2020).

29. J. Weng, X. Han, F. Zeng, Y. Zhang, L. Feng, L. Cai, K. Liang, S. Liu, S. Li, G. Fu, M. Zeng, Y. Gao, Fiber scaffold bioartificial liver therapy relieves acute liver failure and extrahepatic organ injury in pigs. *Theranostics* **11**, 7620–7639 (2021).

30. P. Strnad, F. Tacke, A. Koch, C. Trautwein, Liver—Guardian, modifier and target of sepsis. *Nat. Rev. Gastroenterol. Hepatol.* **14**, 55–66 (2017).

31. F. Beloncle, N. Rousseau, J. F. Hamel, A. Donzeau, A. L. Foucher, M. A. Custaud, P. Asfar, R. Robert, N. Lerolle, Determinants of Doppler-based renal resistive index in patients with septic shock: Impact of hemodynamic parameters, acute kidney injury and predisposing factors. *Ann. Intensive Care* **9**, 51 (2019).

32. T. Nordenfur, K. Caidahl, D. Grishenkov, E. Maksuti, D. Marlevi, M. W. Urban, M. Larsson, Safety of arterial shear wave elastography-ex-vivo assessment of induced strain and strain rates. *Biomed. Phys. Eng. Express* **8**, 055012 (2022).

33. AIUM/NEMA, *Standard for Real-Time Display of Thermal and Mechanical Acoustic Output Indices on Diagnostic Ultrasound Equipment. Revision 2* (AIUM, 2009).

34. B. A. Herman, G. R. Harris, Models and regulatory considerations for transient temperature rise during diagnostic ultrasound pulses. *Ultrasound Med. Biol.* **28**, 1217–1224 (2002).

35. B. W. Cunitz, B. Dunmire, M. R. Bailey, Characterizing the acoustic output of an ultrasonic propulsion device for urinary stones. *IEEE Trans. Ultrason. Ferroelectr. Freq. Control* **64**, 1818–1827 (2017).

36. R. G. Barr, S. R. Wilson, D. Rubens, G. Garcia-Tsao, G. Ferraioli, Update to the society of radiologists in ultrasound liver elastography consensus statement. *Radiology* **296**, 263–274 (2020).

37. M. W. Urban, Production of acoustic radiation force using ultrasound: Methods and applications. *Expert Rev. Med. Devices* **15**, 819–834 (2018).

38. M. A. Kirby, I. Pelivanov, S. Song, L. Ambrozinski, S. J. Yoon, L. Gao, D. Li, T. T. Shen, R. K. Wang, M. O'Donnell, Optical coherence elastography in ophthalmology. *J. Biomed. Opt.* **22**, 1–28 (2017).

39. O. Couture, V. Hingot, B. Heiles, P. Muleki-Seya, M. Tanter, Ultrasound localization microscopy and super-resolution: A state of the art. *IEEE Trans. Ultrason. Ferroelectr. Freq. Control* **65**, 1304–1320 (2018).

40. H. C. Liu, M. Abbasi, Y. H. Ding, T. Roy, M. Capriotti, Y. Liu, S. Fitzgerald, K. M. Doyle, M. Guddati, M. W. Urban, W. Brinjikji, Characterizing blood clots using acoustic radiation force optical coherence elastography and ultrasound shear wave elastography. *Phys. Med. Biol.* **66**, 035013 (2021).

41. H. C. Liu, P. Kijanka, M. W. Urban, Optical coherence tomography for evaluating capillary waves in blood and plasma. *Biomed. Opt. Express* **11**, 1092–1106 (2020).

42. H. C. Liu, P. Kijanka, M. W. Urban, Acoustic radiation force optical coherence elastography for evaluating mechanical properties of soft condensed matters and its biological applications. *J. Biophotonics* **13**, e201960134 (2020).

43. H. C. Liu, P. Kijanka, M. W. Urban, Four-dimensional (4D) phase velocity optical coherence elastography in heterogeneous materials and biological tissue. *Biomed. Opt. Express* **11**, 3795–3817 (2020).

44. W. A. Smith, B. A. Auld, Modeling 1-3 composite piezoelectrics: Thickness-mode oscillations. *IEEE Trans. Ultrason. Ferroelectr. Freq. Control* **38**, 40–47 (1991).

45. K. K. Shung, High frequency ultrasonic imaging. *J. Med. Ultrasound* **17**, 25–30 (2009).

46. J. H. Cha, B. Kang, J. Jang, J. H. Chang, A 15-MHz 1-3 piezocomposite concave array transducer for ophthalmic imaging. *IEEE Trans. Ultrason. Ferroelectr. Freq. Control* **62**, 1994–2004 (2015).

47. K. K. Shung, *Diagnostic Ultrasound: Imaging and Blood Flow Measurements* (CRC Press, 2015).

48. T. A. Ritter, T. R. Shrout, R. Tutwiler, K. K. Shung, A 30-MHz piezo-composite ultrasound array for medical imaging applications. *IEEE Trans. Ultrason. Ferroelectr. Freq. Control* **49**, 217–230 (2002).

49. T. Meeker, Publication and proposed revision of ANSI/IEEE standard 176-1987 "ANSI/IEEE Standard on Piezoelectricity". *IEEE Trans. Ultrason. Ferroelectr. Freq. Control* **43**, 717 (1996).

50. G. Montaldo, M. Tanter, J. Bercoff, N. Benech, M. Fink, Coherent plane-wave compounding for very high frame rate ultrasonography and transient elastography. *IEEE Trans. Ultrason. Ferroelectr. Freq. Control* **56**, 489–506 (2009).

51. C. Kasai, K. Namekawa, A. Koyano, R. Omoto, Real-time two-dimensional blood flow imaging using an autocorrelation technique. *IEEE Trans. Ultrason. Ferroelectr. Freq.* **32**, 458–464 (1985).

52. H. K. Lee, C. B. Capron, H. C. Liu, T. Roy, M. N. Guddati, J. F. Greenleaf, M. W. Urban, Measurement of wave propagation through a tube using dual transducers for elastography in arteries. *Phys. Med. Biol.* **67**, 225010 (2022).

53. X. Zhang, J. F. Greenleaf, Estimation of tissue's elasticity with surface wave speed. *J. Acoust. Soc. Am.* **122**, 2522–2525 (2007).

54. M. Bernal, I. Nenadic, M. W. Urban, J. F. Greenleaf, Material property estimation for tubes and arteries using ultrasound radiation force and analysis of propagating modes. *J. Acoust. Soc. Am.* **129**, 1344–1354 (2011).

55. F. H. Drossaert, A. Giannopoulos, A nonsplit complex frequency-shifted PML based on recursive integration for FDTD modeling of elastic waves. *Geophysics* **72**, T9–T17 (2007).

56. J. A. Jensen, N. B. Svendsen, Calculation of pressure fields from arbitrarily shaped, apodized, and excited ultrasound transducers. *IEEE Trans. Ultrason. Ferroelectr. Freq. Control* **39**, 262–267 (1992).

57. T. L. Szabo, Chapter 1—Introduction, in *Diagnostic Ultrasound Imaging: Inside Out (Second Edition)*, T. L. Szabo, Ed. (Academic Press, 2014), pp. 1–37.

58. B. B. Thomas, R. B. Aramant, S. R. Sadda, M. J. Seiler, Light response differences in the superior colliculus of albino and pigmented rats. *Neurosci. Lett.* **385**, 143–147 (2005).

59. J. Hefler, B. A. Marfil-Garza, R. L. Pawlick, D. H. Freed, C. J. Karvellas, D. L. Bigam, A. M. J. Shapiro, Preclinical models of acute liver failure: A comprehensive review. *PeerJ* **9**, e12579 (2021).

60. T. M. Rahman, H. J. Hodgson, Animal models of acute hepatic failure. *Int. J. Exp. Pathol.* **81**, 145–157 (2000).

61. G. J. Gage, D. R. Kipke, W. Shain, Whole animal perfusion fixation for rodents. *J. Vis. Exp.*, e3564 (2012).

62. Q. Huang, J. Lan, X. Li, Robotic arm based automatic ultrasound scanning for three-dimensional imaging. *IEEE Trans. Industr. Inform.* **15**, 1173–1182 (2019).

63. H. T. Sen, M. A. L. Bell, I. Iordachita, J. Wong, P. Kazanzides, in *2013 IEEE/RSJ International Conference on Intelligent Robots and Systems* (IEEE, 2013), pp. 3071–3076.

64. H. M. Heres, M. Sjoerdsma, T. Schoots, M. C. M. Rutten, F. N. van de Vosse, R. G. P. Lopata, Image acquisition stability of fixated musculoskeletal sonography in an exercise setting: A quantitative analysis and comparison with freehand acquisition. *J. Med. Ultrason.* **47**, 47–56 (2020).

65. R. W. Nuckols, S. Lee, K. Swaminathan, D. Orzel, R. D. Howe, C. J. Walsh, Individualization of exosuit assistance based on measured muscle dynamics during versatile walking. *Sci. Robot.* **6**, eabj1362 (2021).

66. M. Sjoerdsma, C. Caresio, B. Tchang, A. Meeder, F. van de Vosse, R. Lopata, The feasibility of dynamic musculoskeletal function analysis of the vastus lateralis in endurance runners using continuous, hands-free ultrasound, hands-free ultrasound. *Appl. Sci.* **11**, 1534 (2021).